International Journal of Hydrogen Energy 278 (2026) 157644

Contents lists available at ScienceDirect

International Journal of Hydrogen Energy

journal homepage: www.elsevier.com/locate/he

Capacity configuration method for hybrid electro-hydrogen storage in islanded energy systems based on quantum-inspired optimization

Shizhao Wang [a], Zhenhao Weng [a], Ruichong Li [a], Longze Wang [a,*], Jingren Zhou [a], Zehan Li [a], Meicheng Li [a,b,**]

[a] State Key Laboratory of Alternate Electrical Power System with Renewable Energy Sources, School of New Energy, North China Electric Power University, Beijing, 102206, China

[b] College of Automotive and Energy Engineering, Tongji University, Shanghai, 201804, China

ARTICLE INFO

Keywords:
Capacity configuration
Multi-objective optimization
Quantum inspired
Energy management strategy

ABSTRACT

The differences in power response and long-duration support across storage units complicate capacity configuration for both supply reliability and renewable energy utilization. This paper proposes a quantum-inspired capacity configuration method for hybrid electro-hydrogen storage in islanded energy systems. First, a dual-pressure hydrogen storage structure is designed to mitigate short-term fluctuations and enable long-term energy shifting. Second, a dynamic quantum-threshold energy management strategy (DQT-EMS) is developed to coordinate the battery and dual-pressure hydrogen storage. Finally, a multi-objective optimization model based on year-scale operational simulation is solved using a Quantum multi-objective parrot optimization (QMOPO) to generate Pareto fronts. Case studies show that the proposed method enhances short-term balancing and seasonal hydrogen-based energy shifting while increasing renewable energy utilization to 99.20%. The hypervolume achieved by QMOPO is 6.70% higher than that of MOPSO. Moreover, DQT-EMS reduces electrolyzer and fuel cell start-stop frequencies by 5.94% and 26.13%, respectively, significantly enhancing operational continuity and smoothness.

1. Introduction

1.1. Motivation

In remote islands and mountainous areas where grid extension is impractical, distributed wind and photovoltaic generation can provide clean electricity for islanded power systems [1,2]. However, the intermittent and fluctuating nature of renewable generation can easily disturb the power balance, thereby undermining the continuity and stability of power supply [3,4]. Therefore, deploying energy storage is essential for mitigating renewable-power fluctuations, maintaining stable system operation, and ensuring a reliable electricity supply.

Electro-hydrogen integrated energy storage systems (EH-IES) provide an effective solution to this challenge [5–7]. Electrochemical storage features a fast response and is well suited for short-timescale power smoothing. In contrast, hydrogen energy storage offers high energy density and long-duration storage capability, which makes it more suitable for energy shifting across days, weeks, and even seasons [8–10]. However, in the islanded EH-IES, the capacities of batteries, electrolyzers, fuel cells, and different hydrogen storage units are strongly coupled, and their capacity must balance investment cost, power-supply reliability, and renewable-energy utilization [11–14]. Therefore, coordinated capacity configuration of the islanded EH-IES is of great importance.

1.2. Literature review

(1) *Capacity configuration of energy storage systems*

In an EH-IES, capacity configuration determines investment scale, operational flexibility, and long-term profitability, and therefore constitutes a key step toward cost-effective operation. Existing research has mainly focused on optimization objectives and system configurations. Reference [15] minimizes the total net present cost while modeling

* Corresponding author.
** Corresponding author.
E-mail addresses: 120242211126@ncepu.edu.cn (S. Wang), 120252111026@ncepu.edu.cn (Z. Weng), 120242211004@ncepu.edu.cn (R. Li), lzwang@ncepu.edu.cn (L. Wang), 120231100617@ncepu.edu.cn (J. Zhou), 120232111033@ncepu.edu.cn (Z. Li), mcli@ncepu.edu.cn (M. Li).

https://doi.org/10.1016/j.ijhydene.2026.157644
Received 28 April 2026; Received in revised form 23 August 2026; Accepted 16 September 2026
Available online 25 September 2026
0360-3199/© 2026 Hydrogen Energy Publications LLC. Published by Elsevier Ltd. All rights are reserved, including those for text and data mining, AI training, and similar technologies.

reliability via a loss-of-power-supply probability constraint, demonstrating that such a formulation can simultaneously control cost and improve reliability. Reference [16] couples the levelized cost of electricity (LCOE) with the maximization of effective load carrying capability (ELCC), enabling a more comprehensive evaluation of economic performance and operational adequacy for capacity planning. Reference [17] formulates an objective function that combines total revenue and supply reliability, and determines the optimal capacity mix through coordinated multi-variable optimization. Reference [18] develops a bi-level framework, where the upper level minimizes economic cost and the lower level minimizes carbon-related costs, thereby coordinating economic and environmental benefits. Reference [19] proposes a bi-level multi-timescale model with a rolling optimization mechanism, minimizing energy imbalance at the upper level and electricity purchase cost at the lower level, which enhances both robustness and economic performance. Despite the progress made in recent studies, important limitations remain in both multi-objective formulation and the modeling of hydrogen storage characteristics. On the one hand, most studies are still dominated by economic objectives, whereas reliability and environmental performance are typically treated as constraints, weakening the balanced characterization of multi-objective trade-offs. On the other hand, the hydrogen storage pressure is rarely linked explicitly to storage duration, which limits the use of hydrogen storage flexibility across timescales.

(2) *Energy management strategies*

Energy management strategies determine the operational implementability and regulation effectiveness of EH-IES. Their core task is to allocate power and regulate device states so that electrochemical storage, hydrogen production/storage, and FC conversion can operate in a coordinated manner while adapting to time-varying source–load conditions. To meet the operational requirements of EH-IES, a variety of control and optimization strategies have been developed to enhance system stability and resource utilization. Reference [20] combines wavelet decomposition with particle swarm optimization, where wavelet decomposition is used to capture the multi-scale characteristics of non-stationary data and particle swarm optimization is employed to solve the capacity configuration problem. Reference [21] employs a finite-state-machine control system with four operating modes to coordinate power balance and device states, while establishing an integrated sizing-control framework with the minimization of the levelized cost of hydrogen as the objective, thereby balancing hydrogen utilization efficiency and economic performance. Reference [22] proposes an operating control strategy based on lithium-battery SOC feedback, which helps ensure the safety and stability of the storage unit. Reference [23] proposes a dynamic scheduling framework that adjusts charging and discharging actions in response to real-time power imbalance, thus mitigating fluctuations and enhancing grid stability. Reference [24] develops a bi-level optimization framework using an adaptive greedy search algorithm, in which the upper level determines the optimal storage power and the lower level derives the corresponding capacity configuration across multiple scenarios. However, current energy management strategies remain limited. Most are based on conventional priority rules and fixed power allocation logic, which hinders deep coordination among heterogeneous storage units such as lithium batteries and hydrogen storage. Meanwhile, frequent start-stop operation of the EL and FC restricts the effective exploitation of the complementary characteristics of different storage technologies.

(3) *Solution algorithms*

EH-IES optimization models are typically characterized by multiple objectives, multiple constraints, and high-dimensional decision variables, with strong coupling among variables. The performance of solution algorithms directly affects solution accuracy, computational efficiency, and the quality of Pareto-optimal solutions. Therefore, developing efficient and robust algorithms remains a central research topic. Existing work mainly relies on heuristic or hybrid algorithms, whose effectiveness has been validated under various scenarios. Reference [25] applies a continuous grey wolf optimizer (CGWO) to capacity configuration and reports improved economic and reliability performance compared with conventional particle swarm optimization and grey wolf optimization. Reference [26] generates nine qualified representative scenarios using a deep-learning gradient-penalty generative model and then solves the system model via the sparrow search algorithm, effectively reducing renewable curtailment. Reference [27] considers economic, environmental, and reliability objectives and employs a multi-objective grey wolf optimizer to obtain the optimal capacity configuration. Reference [28] develops a bi-level capacity and operation co-optimization model for a wind-solar-hydrogen multi-energy system and adopts a hybrid NSGA-II and linear programming approach, which reduces system cost and improves energy utilization. However, conventional heuristics can be trapped in local optima under complex constraints and high-dimensional search spaces, making it difficult to stably obtain high-quality solution sets. This may bias configuration decisions and further deteriorate subsequent operational performance.

In recent years, quantum-inspired algorithms have shown potential advantages over classical heuristics in multi-objective optimization and constrained problem solving. In high-dimensional and strongly coupled search spaces, quantum-inspired search may improve global exploration and reduce the risk of premature convergence. Reference [15] proposes a quantum beluga whale optimization algorithm (QBWO) for capacity configuration under generation-cost uncertainty and reliability constraints, achieving cost reduction while satisfying reliability requirements. Reference [29] studies coordinated scheduling of microgrid clusters and shared energy storage in active distribution networks, formulates a leader–follower game, and solves the equilibrium using quantum particle swarm optimization (QPSO) embedded with CPLEX. The results indicate that quantum-inspired algorithms can improve solution performance when multi-agent interactions and complex constraints coexist. Reference [30] develops an improved multi-objective dragonfly algorithm with quantum-behavior enhancement for industrial-process optimization, showing favorable global convergence and local search capability in terms of the inverted generational distance metric. Overall, existing algorithms still face key bottlenecks. Hence, it remains necessary to develop new algorithms with stronger global search capability, higher computational efficiency, and improved stability to support reliable solutions for islanded EH-IES optimization problems.

1.3. Research gaps

Based on the above analysis, existing studies still exhibit the following three limitations.

(1) Most existing studies model hydrogen storage using a single pressure level or a fixed storage mode, while the coordinated matching between storage duration and pressure level remains insufficiently addressed. In islanded systems, where hydrogen plays a key role in long-duration energy shifting, neglecting this distinction may lead to additional compression costs and suboptimal storage allocation.
(2) For islanded energy systems with heterogeneous storage units, current energy management strategies still mainly rely on fixed priorities or heuristic operating rules. Such methods cannot fully capture the multi-timescale complementarity between electrochemical and hydrogen storage, and may induce frequent start-stop operations of key devices such as EL and FC.
(3) Capacity configuration of hybrid electro-hydrogen storage is a high-dimensional multi-objective problem coupled with long-

horizon sequential simulation. Conventional heuristic algorithms often struggle to balance convergence quality, computational efficiency, and Pareto-set diversity, while the application of quantum-inspired optimization methods to this problem remains limited.

1.4. Contributions and paper organization

To address the above gaps, this paper investigates a quantum-inspired capacity configuration method for hybrid electro-hydrogen storage in islanded energy systems. The main contributions are summarized as follows.

(1) **Dual-pressure hydrogen storage design:** An islanded energy system framework is established in which electrochemical storage and dual-pressure hydrogen storage are jointly incorporated into the capacity configuration process. By distinguishing low-pressure and high-pressure hydrogen storage, the proposed design captures the coordinated matching between storage duration and pressure level.
(2) **Dynamic quantum-threshold modeling:** A dynamic quantum-threshold (DQT) model is proposed to generate state-adaptive operating thresholds for electro-hydrogen coordination. Based on this, the DQT-EMS is embedded into the capacity configuration framework to explicitly couple short-term operating decisions with long-term capacity planning.
(3) **Quantum-inspired multi-objective optimization algorithm:** A quantum multi-objective parrot optimization algorithm (QMOPO) is developed to solve the resulting multi-objective capacity configuration problem. Quantum-inspired behavior selection and adaptive rotation updating are introduced to improve convergence performance and enhance diversity preservation of the Pareto solution set.

The remainder of this paper is organized as follows. Section 2 presents the modeling framework of the islanded EH-IES. Section 3 formulates the objective functions and develops the energy management strategy. Section 4 introduces the proposed QMOPO-based solution method. Section 5 reports the case studies and comparative analysis. Section 6 concludes the paper and outlines future work.

2. System framework

2.1. System structure of the islanded EH-IES

The islanded EH-IES consists of a wind turbine (WT), photovoltaic (PV) array, electrolyzer (EL), fuel cell (FC), battery energy storage (BES), low-pressure hydrogen storage (LPHS), high-pressure hydrogen storage (HPHS), a compressor, a transformer, and local loads. Wind and PV serve as the primary energy sources to support local electricity demand. As an islanded system, electricity is not imported from an external grid, and surplus renewable generation is curtailed when it cannot be absorbed by internal devices. When renewable generation is surplus, electricity is first used to meet the load. Subject to BES charging constraints, the remaining power is then allocated to the electrolyzer for hydrogen production. The produced hydrogen is dispatched to LPHS and HPHS according to operating conditions and scheduling requirements. Specifically, LPHS mainly provides intra-day and short-cycle buffering to mitigate fluctuations, whereas HPHS focuses on long-cycle and inter-seasonal energy shifting to ensure long-term energy adequacy.

When renewable generation is insufficient, the BES delivers fast power support to address deficits and fluctuations from the second-to-hour timescale. If the energy shortfall persists or evolves into a long-duration deficit, stored hydrogen is converted back to electricity through the fuel cell. The fuel cell output then collaborates with the BES to supply the load, ensuring continuity of service and supply reliability. The operation of the islanded EH-IES is coordinated by DQT-EMS. This strategy continuously monitors wind and PV generation, load level, and the operating states of BES, LPHS, and HPHS, while dynamically updating the start-stop decisions and power setpoints of the electrolyzer, as well as the power output of the fuel cell. In this way, the islanded EH-IES achieves coordinated regulation of electricity flows, hydrogen flows, and control information across multiple timescales, thereby enhancing operational stability and resource utilization. The overall system structure is illustrated in Fig. 1.

2.2. Component models

The energy supply subsystem includes PV generation and WT generation. The PV output power is mainly influenced by solar irradiance and temperature. It can be expressed as Eqs. (1) and (2):

$$P_{pv}(t) = P_{STC}\frac{G(t)}{G_{STC}}[1 + k(T_a(t) - T_{STC})] \tag{1}$$

$$T_a(t) = T_{amb}(t) + 0.0256\, G(t) \tag{2}$$

where $P_{pv}(t)$ denotes the PV output power at time t. P_{STC} is the rated PV power under standard test conditions (STC). $G(t)$ and G_{STC} denote the solar irradiance at time t and under STC. k is the power temperature coefficient. $T_a(t)$ and T_{STC} denote the actual temperature and the temperature under STC. $T_{amb}(t)$ denotes the ambient temperature.

The WT output power depends on the turbine characteristics and the wind speed at hub height. It can be expressed as Eq. (3):

$$P_{wt}(t) = \begin{cases} 0, & v(t) < v_{in} \text{ or } v(t) > v_{out} \\ P_r\dfrac{v(t) - v_{in}}{v_r - v_{in}}, & v_{in} \le v(t) \le v_r \\ P_r, & v_r \le v(t) \le v_{out} \end{cases} \tag{3}$$

where $P_{wt}(t)$ denotes the WT output power at time t. P_r is the rated WT power. $v(t)$ denotes the wind speed at hub height. v_{in}, v_r, v_{out} denote the cut-in, rated, cut-out wind speeds.

The energy conversion subsystem includes EL and FC. When renewable generation is surplus, EL is activated to produce hydrogen, which can be stored in the low-pressure or high-pressure hydrogen storage tank. In the cascade hydrogen storage structure, the electric power of the hydrogen production and storage process is divided according to the hydrogen storage pressure level. The low-pressure and high-pressure storage paths correspond to different comprehensive conversion efficiencies because the compression-related auxiliary power consumption varies with the storage pressure level. Therefore, the hydrogen production mass can be expressed as Eq. (4):

$$\begin{cases} P_{ele}(t) = P_{LH_2,ele}(t) + P_{HH_2,ele}(t) \\ m_{LH_2,ele}(t) = \dfrac{\eta_{LH_2,ele}\, P_{LH_2,ele}(t)\Delta t}{LHV_{H_2}} \\ m_{HH_2,ele}(t) = \dfrac{\eta_{HH_2,ele}\, P_{HH_2,ele}(t)\Delta t}{LHV_{H_2}} \end{cases} \tag{4}$$

where $P_{ele}(t)$ denotes the total EL power at time t. $P_{LH_2,ele}(t)$ and $P_{HH_2,ele}(t)$ denote the EL power corresponding to the low-pressure and high-pressure hydrogen storage paths. $m_{LH_2,ele}(t)$ and $m_{HH_2,ele}(t)$ denote the hydrogen production mass stored in the low-pressure and high-pressure

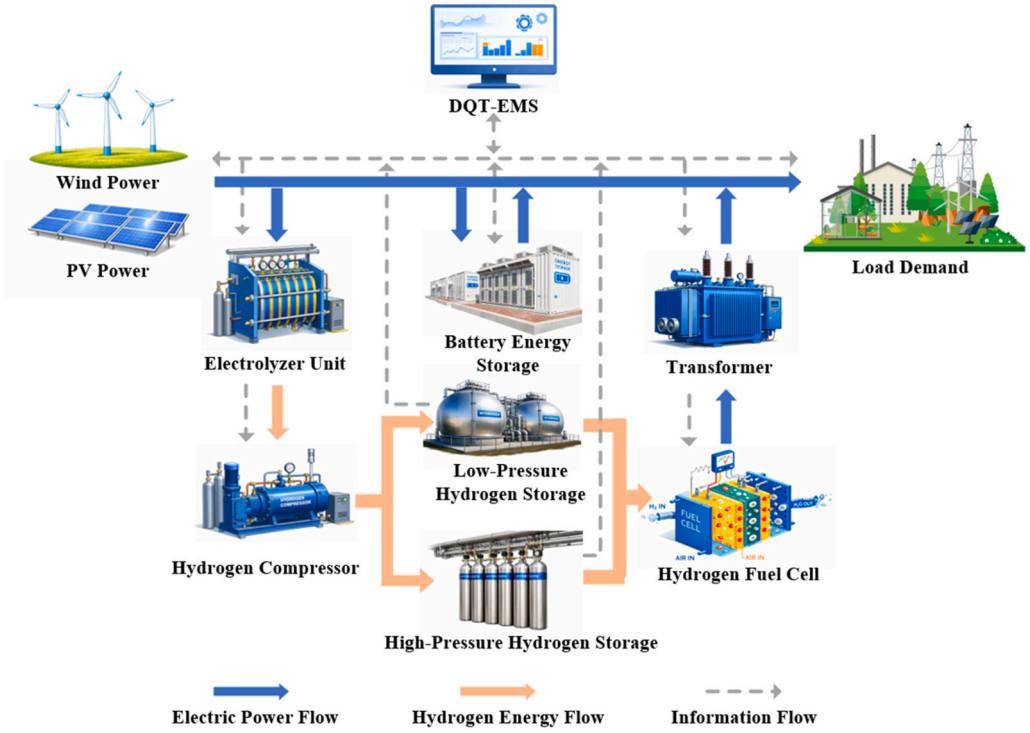


Fig. 1. Framework of the islanded EH-IES.

hydrogen storage tanks at time t. $\eta_{LH_2,ele}$ and $\eta_{HH_2,ele}$ denote the pressure-level-related conversion efficiencies of the two storage paths, which include the effects of electrolysis efficiency and compression-related auxiliary power consumption. Since the high-pressure storage path requires a higher compression level, $\eta_{HH_2,ele}$ is generally lower than $\eta_{LH_2,ele}$. LHV_{H_2} denotes the lower heating value of hydrogen, and Δt denotes the time interval.

When renewable generation is insufficient, FC is activated to consume hydrogen and generate electricity to meet the load demand. The hydrogen consumption mass is mainly determined by the FC power and the conversion efficiency. It can be expressed as Eq. (5):

$$m_{H_2,fc}(t) = \frac{P_{fc}(t)\Delta t}{\eta_{fc} LHV_{H_2}} \tag{5}$$

where $m_{H_2,fc}(t)$ denotes the hydrogen consumption mass at time t. $P_{fc}(t)$ denotes the FC power at time t. η_{fc} denotes the conversion efficiency.

The energy storage units include BES, LPHS, and HPHS. BES undertakes intra-day and real-time balancing tasks, mainly by fast charging and discharging to satisfy short-timescale load demand and accommodate fluctuating renewable generation. Its charging/discharging behavior can be expressed as Eq. (6) and Eq. (7):

$$P_{SC}(t) = \eta_{dis,SC} P_{SC}^{dis}(t) - \frac{P_{SC}^{ch}(t)}{\eta_{ch,SC}} \tag{6}$$

$$SOC_{SC}(t) = SOC_{SC}(t-1) + \frac{\eta_{ch} P_{SC}^{ch}(t)\Delta t}{E_{SC}^{cap}} - \frac{P_{SC}^{dis}(t)\Delta t}{\eta_{dis} E_{SC}^{cap}} \tag{7}$$

where $P_{SC}(t)$ denotes the operating power of the battery at time t. A positive $P_{SC}(t)$ indicates battery discharging, whereas a negative $P_{SC}(t)$ indicates battery charging. $P_{SC}^{ch}(t)$ denotes the charging power of the battery at time t. $P_{SC}^{dis}(t)$ denotes the discharging power of the battery at time t. $\eta_{ch,SC}$ and $\eta_{dis,SC}$ denote the energy loss rates during battery charging and discharging, respectively. $SOC_{SC}(t)$ denotes the state of charge of the battery. E_{SC}^{cap} denotes the rated capacity of the battery.

The hydrogen storage units in the islanded EH-IES consist of low-pressure hydrogen storage (LPHS) and high-pressure hydrogen storage (HPHS). Since both units store the same energy carrier, their hydrogen storage states follow the same mass-conservation-based SOC update equation. In the proposed dual-pressure structure, LPHS is mainly used for short- and medium-term hydrogen buffering under frequent renewable-power fluctuations. HPHS is mainly used for long-duration hydrogen reserve and seasonal energy shifting during prolonged renewable-power shortages. The hydrogen storage behavior of LPHS and HPHS can be expressed as Eq. (8):

$$SOC_{H_2}(t) = SOC_{H_2}(t-1) + \left(\frac{\eta_{ch,H_2} m_{in}(t)}{M^{cap}} - \frac{m_{out}(t)}{\eta_{dis,H_2} M^{cap}}\right)\Delta t - \gamma SOC_{H_2}(t-1)\Delta t \tag{8}$$

where $SOC_{H_2}(t)$ denotes the hydrogen storage state at time t. $m_{in}(t)$ and $m_{out}(t)$ denote the hydrogen mass flow rates entering and leaving the storage unit at time t. η_{ch,H_2} and η_{dis,H_2} denote the hydrogen charging and discharging efficiencies. M^{cap} denotes the rated hydrogen storage capacity. γ denotes the leakage loss rate. In general, the charging efficiency of the LPHS is 0.92–0.98. The discharging efficiency is 0.94~0.99. The leakage loss rate is 1×10^{-6}~1×10^{-5}. The charging efficiency of HPHS is 0.85–0.92. The discharging efficiency is 0.88–0.95. The leakage loss rate is 5×10^{-6}~5×10^{-5} [31].

In the proposed dual-pressure hydrogen storage structure, LPHS and HPHS are distinguished by their operational roles, efficiency parameters, leakage loss rates, and economic characteristics [32]. LPHS is mainly used for frequent short- and medium-term hydrogen buffering because of its lower pressure-bearing requirement, lower unit capacity

cost, and higher charging/discharging efficiency. By contrast, HPHS is mainly used for long-duration hydrogen reserve and seasonal energy shifting because of its higher storage density and stronger support capability during prolonged renewable power shortages. These differences are incorporated into the capacity configuration model through the charging/discharging efficiency coefficients, leakage loss rates, unit capacity costs, and the corresponding dispatch roles in DQT-EMS.

2.3. Constraint condition

The operation of the islanded EH-IES is constrained by the system power balance, device operating limits, storage-state bounds, and the operating logic of key devices. Specifically, the total power supplied by the PV, WT, BES, and FC must satisfy the load demand, as well as the charging power of the BES and the power consumed by the EL, as expressed in Eq. (9). In addition, the output powers of the WT and PV, together with the charging/discharging power of the BES and the operating powers of the EL and FC, are all restricted within their respective allowable ranges. To further ensure the engineering feasibility of key device operation, the ramping constraints of the EL and FC are also considered, as given in Eq. (10). Moreover, the EL and FC are required to follow the corresponding start-stop logic and minimum on/off time requirements in practical dispatch, so as to avoid frequent switching and improve operational continuity. The storage states of the BES, LPHS, and HPHS must remain within their prescribed capacity limits. Meanwhile, the BES is restricted from charging and discharging simultaneously, and the EL and FC are restricted from operating simultaneously, as shown in Eq. (11) and Eq. (12).

$$P_{pv}(t)+P_{wt}(t)+P_{bd}(t)+P_{fc}(t)=P_{load}(t)+P_{bc}(t)+P_{ele}(t) \tag{9}$$

$$\begin{cases} 0 \le P_{pv}(t) \le P_{pv}^{max}(t) \\ 0 \le P_{wt}(t) \le P_{wt}^{max}(t) \\ 0 \le P_{sc,in}(t) \le P_{sc,in}^{max}(t) \\ 0 \le P_{sc,out}(t) \le P_{sc,out}^{max}(t) \\ P_{ele}^{min}(t) \le P_{ele}(t) \le P_{ele}^{max}(t) \\ P_{fc}^{min}(t) \le P_{fc}(t) \le P_{fc}^{max}(t) \\ -R_{ele}^{down} \le P_{ele}(t)-P_{ele}(t-1) \le R_{ele}^{up} \\ -R_{fc}^{down} \le P_{fc}(t)-P_{fc}(t-1) \le R_{fc}^{up} \end{cases} \tag{10}$$

$$\begin{cases} SOC_{SC}^{min} \le SOC_{SC}(t) \le SOC_{SC}^{max} \\ SOC_{LH_2}^{min} \le SOC_{LH_2}(t) \le SOC_{LH_2}^{max} \\ SOC_{HH_2}^{min} \le SOC_{HH_2}(t) \le SOC_{HH_2}^{max} \end{cases} \tag{11}$$

$$\begin{cases} u_{bc}(t)+u_{bd}(t) \le 1 \\ u_{ele}(t)+u_{fc}(t) \le 1 \end{cases} \tag{12}$$

where $SOC_{SC}(t)$, $SOC_{LH_2}(t)$, and $SOC_{HH_2}(t)$ denote the storage states of BES, LPHS, and HPHS at time t. R_{ele}^{up} and R_{ele}^{down} denote the upward and downward ramping limits of the EL. R_{fc}^{up} and R_{fc}^{down} denote the upward and downward ramping limits of the FC. $u_{bc}(t)$ and $u_{bd}(t)$ denote the charging and discharging states of the BES. $u_{ele}(t)$ and $u_{fc}(t)$ denote the operating states of the EL and FC. These state variables are binary variables.

3. Multi-objective optimization model

3.1. Objective functions

$$\min \mathbf{F}=[F_1,F_2,F_3] \tag{13}$$

where $\mathbf{F}$ denotes the multi-objective function vector. F_1, F_2, and F_3 denote the economic objective, reliability objective, and environmental objective.

The economic objective considered in this paper is to minimize the total life-cycle cost of the system (TLCC), which can be expressed as Eq. (14):

$$\begin{cases} F_1 = C_{cap}+C_{om}+C_{rep} \\ C_{cap} = \sum_i \left[\dfrac{r(1+r)^{LT_i}}{(1+r)^{LT_i}-1}\right]\cdot\left(c_{e,i}\cdot E_i + c_{p,i}\cdot P_i\right) \\ C_{om} = \sum_{t=1}^{T} \dfrac{C_{om,t}^{base}+C_{om,t}^{op}+C_{om,t}^{ss}}{(1+r)^t} \\ C_{rep} = \sum_{i=1}^{n} C_{rep,i} \end{cases} \tag{14}$$

where C_{cap} denotes the investment cost. C_{om} denotes the aggregated operation and maintenance cost. Specifically, $C_{om,t}^{base}$, $C_{om,t}^{op}$ and $C_{om,t}^{ss}$ denote the basic maintenance cost, operation-related maintenance cost, and start–stop-related maintenance and lifetime-loss cost. $C_{om,t}^{ss}$ is used to reflect the potential maintenance and degradation effects associated with frequent start–stop behavior of EL and FC. C_{rep} denotes the equipment replacement cost. $c_{e,i}$ denotes the unit capacity cost of the i-th device. E_i denotes the capacity of the i-th device. $c_{p,i}$ denotes the unit power cost of the i-th device. P_i denotes the rated power of the i-th device. r denotes the discount rate. LT_i denotes the lifetime of the i-th device.

The reliability objective is to minimize the loss of power supply probability (LPSP), which is calculated as the ratio of the total unmet load to the total load demand, as expressed in Eq. (15):

$$F_2=\frac{\sum_{t=1}^{n} P_{dump}(t)}{\sum_{t=1}^{n} P_{load}(t)}=\frac{\sum_{t=1}^{n}\left(P_{load}(t)-P_{pv}(t)-P_{wt}(t)-P_{bd}(t)-P_{fc}(t)\right)}{\sum_{t=1}^{n} P_{load}(t)} \tag{15}$$

where $P_{dump}(t)$ denotes the power shortage of the system at time t. $P_{load}(t)$ denotes the load power at time t. $P_{pv}(t)$ denotes the PV output power at time t. $P_{wt}(t)$ denotes the WT output power at time t. $P_{bd}(t)$ denotes the BES discharging power at time t. $P_{fc}(t)$ denotes the FC output power at time t.

The environmental objective considered in this paper is to maximize the renewable energy utilization rate. For ease of calculation, it is transformed into a minimization objective by minimizing the renewable energy curtailment rate (CUR), which can be expressed as Eq. (16):

$$F_3=\frac{\sum_{t=1}^{n} P_{loss}(t)}{\sum_{t=1}^{n}\left(P_{pv}(t)+P_{wt}(t)\right)}=\frac{\sum_{t=1}^{n}\left(P_{pv}(t)+P_{wt}(t)-P_{load}(t)-P_{bc}(t)-P_{ele}(t)\right)}{\sum_{t=1}^{n}\left(P_{pv}(t)+P_{wt}(t)\right)} \tag{16}$$

where $P_{loss}(t)$ denotes the curtailed renewable power of the system at time t. $P_{bc}(t)$ denotes the BES charging power at time t. $P_{ele}(t)$ denotes the input power of EL at time t.

3.2. Dynamic quantum-threshold energy management strategy

In the islanded EH-IES, considering the coordinated operation of multiple devices and the start-stop constraints, this paper constructs a system-state energy management strategy. The system-state vector is defined as Eq. (17):

$$X(t)=[SOC_{SC}(t),SOC_{LH_2}(t),SOC_{HH_2}(t),P_{net}(t)]^T \tag{17}$$

where the net power $P_{net}(t)$ represents the power balance between renewable generation and load demand:

$$P_{net}(t) = P_{pv}(t) + P_{wt}(t) - P_{load}(t) \tag{18}$$

To provide a consistent power scale for different capacity configuration schemes and realize scenario-adaptive partitioning, a dynamic quantum-threshold function is introduced:

$$P_{th}^{dyn}(t) = f(x(t), u) = \alpha(t)P_{SC,\max} + \beta(t)P_{EL,\max} + \gamma(t)P_{FC,\max} \tag{19}$$

where $P_{SC,\max}$, $P_{EL,\max}$, and $P_{FC,\max}$ denote the rated powers of the battery, electrolyzer, and fuel cell, respectively. $\alpha(t)$, $\beta(t)$, and $\gamma(t)$ denote the relative contributions of the three devices to the threshold construction, thereby incorporating the rated power scales of different devices into a unified capacity-dependent triggering scale. Considering that the participation mechanisms of the three devices under surplus/deficit conditions are different and mutually exclusive logic exists (i.e., EL and FC are not activated simultaneously), quantum-inspired rotation-gate parameterization is adopted to obtain the weighting coefficients that satisfy non-negativity and normalization constraints. First, define the single-qubit rotation gate and controlled rotation gate as Eq. (20) and Eq. (21):

$$R_y(\theta) = \begin{bmatrix} \cos\frac{\theta}{2} & -\sin\frac{\theta}{2} \\ \sin\frac{\theta}{2} & \cos\frac{\theta}{2} \end{bmatrix} \tag{20}$$

$$CR_y(\theta_2) = \begin{bmatrix} 1 & 0 & 0 & 0 \\ 0 & 1 & 0 & 0 \\ 0 & 0 & \cos\frac{\theta_2}{2} & -\sin\frac{\theta_2}{2} \\ 0 & 0 & \sin\frac{\theta_2}{2} & \cos\frac{\theta_2}{2} \end{bmatrix} \tag{21}$$

Starting from the initial state $|00\rangle$, construct the threshold quantum state as Eq. (22):

$$|\psi(t)\rangle = CR_y(\theta_2(t))\left(R_y(\theta_1) \otimes I\right)|00\rangle \tag{22}$$

According to the Born rule, the measurement probabilities of the quantum state are defined as the threshold coefficients:

$$\begin{cases} \alpha(t) &= |\langle 00|\psi(t)\rangle|^2 \\ \beta(t) &= |\langle 10|\psi(t)\rangle|^2 \\ \gamma(t) &= |\langle 11|\psi(t)\rangle|^2 \end{cases} \tag{23}$$

From Eqs. (20)–(23), it can be obtained that:

$$\begin{cases} \alpha(t) &= \cos^2\frac{\theta_1}{2} \\ \beta(t) &= \sin^2\frac{\theta_1}{2}\cos^2\frac{\theta_2(t)}{2} \\ \gamma(t) &= \sin^2\frac{\theta_1}{2}\sin^2\frac{\theta_2(t)}{2} \\ \theta_2(t) &= \pi(1 - \mathrm{H}(P_{net}(t))) \end{cases} \tag{24}$$

where $\mathrm{H}(P_{net}(t))$ denotes the Heaviside function, which is used to map the sign of the net power to the weighting allocation within the hydrogen path, thereby embedding the mutual participation mechanism of EL/FC at the coefficient level. It should be emphasized that $P_{th}^{dyn}(t)$ is used to construct a normalized scale without changing the power-balance relationship and device operating constraints. Accordingly, the normalized net power is defined as Eq. (25):

$$r(t) = \frac{P_{net}(t)}{P_{th}^{dyn}(t)} \tag{25}$$

To realize scenario-adaptive partitioning of operating conditions, a triangular membership function is used to map the continuous variable into six discrete scenarios:

$$\mu_i(r) = \max\left(0, 1 - \frac{|r - c_i|}{\delta_i}\right), i = 1, 2, 3, 4, 5, 6 \tag{26}$$

where c_i and δ_i denote the center and width parameters of the i-th scenario, respectively. The scenario selection follows the maximum membership criterion:

$$S^* = \arg\max_{i=1}^{6} \mu_i(r) \tag{27}$$

Specifically, after the scenario decision set is selected according to the maximum membership principle, the feasibility of the corresponding device operation is further checked. The activation of EL and FC is jointly determined by the net-power condition and the fuzzy scenario-selection result [33]. For EL, when the system has renewable-power surplus, EL is activated only when the available net power is higher than its minimum operating power and the corresponding surplus scenario has the highest membership degree. For FC, when the system has a power deficit, FC is activated only when the power shortage is higher than its minimum operating power and the corresponding deficit scenario has the highest membership degree. If these conditions are not satisfied, the feasible scenario is selected according to the descending order of membership. In this way, EL and FC are not immediately triggered by slight net-power fluctuations around the threshold, which helps reduce frequent start-stop operations of EL and FC.

The above rule establishes a direct link between the mathematical structure of DQT-EMS and the actual dispatch of the hybrid storage system. The rotation-gate parameterization and Born-rule measurement generate normalized weighting coefficients according to the rated capacities of BES, EL, and FC. Therefore, the dynamic threshold changes with different capacity configuration schemes. The Heaviside function identifies the surplus or deficit direction of the net power. Under surplus conditions, BES is used for fast power absorption and EL is used for hydrogen production when the surplus is sufficient. Under deficit conditions, BES provides fast power compensation and FC is activated when the deficit is sufficiently large. The triangular membership function further divides the operating state into slight, moderate, and large surplus or deficit scenarios. Based on these scenarios, BES mainly responds to short-term power fluctuations, LPHS supports short- and medium-term hydrogen buffering, and HPHS provides long-duration hydrogen reserve. The overall workflow of the proposed DQT-EMS is shown in Fig. 2.

4. QMOPO solution algorithm

4.1. Quantum enhancement of parrot operators

The solution process of parrot optimizer (PO) relies on four behaviors: foraging, staying, communicating, and fearing strangers. In the conventional PO algorithm, these behaviors are selected with equal probabilities. Although PO can exhibit different performance across optimization problems when different behavior-selection probabilities are adopted, such probabilities are not optimal for the specific problem under consideration. In this study, quantum computing and an adaptive strategy are introduced to enable behavior selection in the algorithm [34].

To realize the adaptive selection of the four behavior operators during the iterative process, this paper treats "foraging, staying, communicating, and fearing strangers" as a set of mutually orthogonal behavior bases and introduces a behavior-selection quantum state:

$$|S\rangle = \sum_{i=1}^{4} \alpha_i e^{i\varphi_i}|s_i\rangle \tag{28}$$

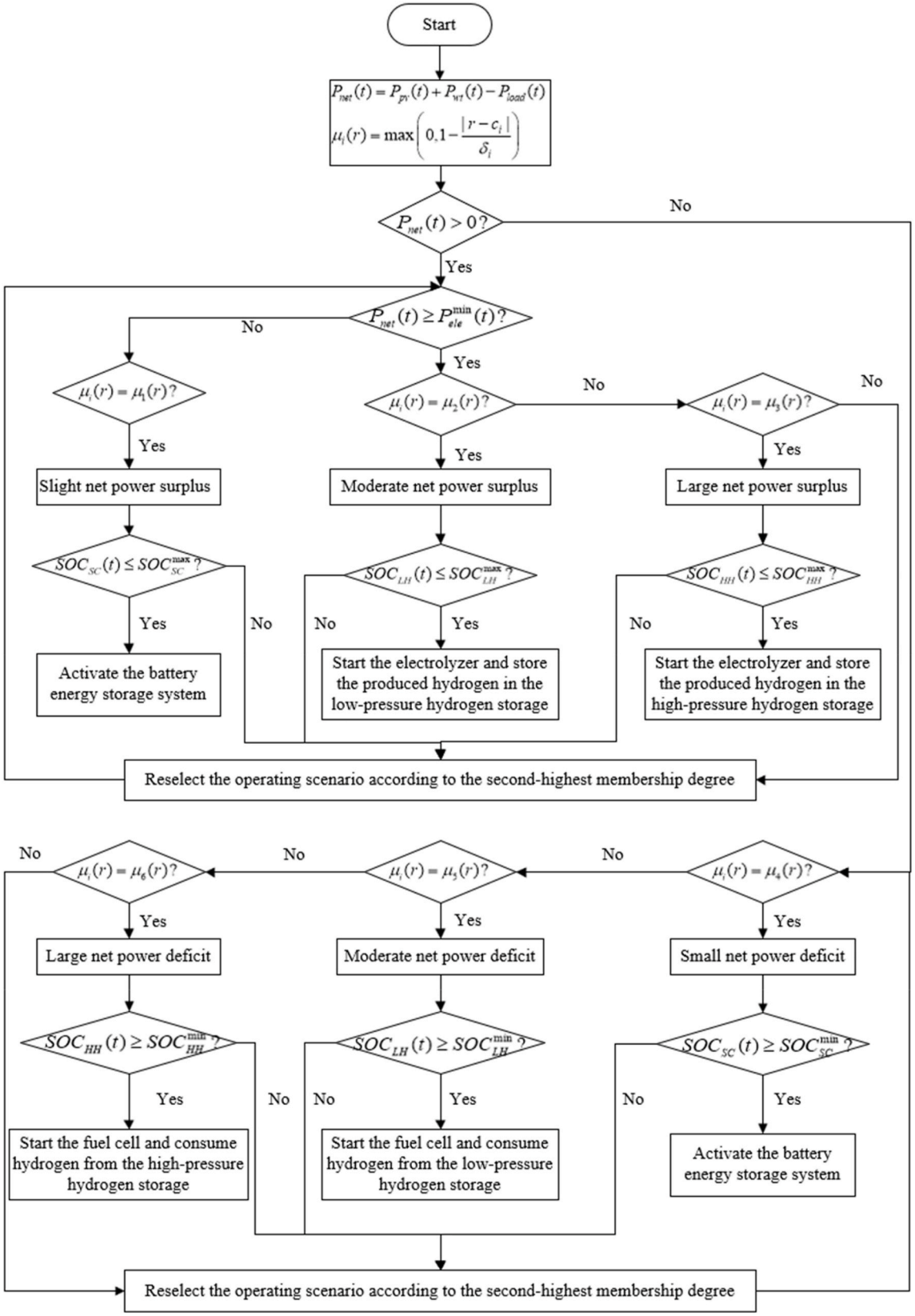


Fig. 2. Flowchart of the proposed DQT-EMS for the islanded EH-IES. By integrating a dynamic power threshold with fuzzy logic, the operating state is classified into six dynamic scenarios, including slight, moderate, and large net power surplus, as well as slight, moderate, and large net power deficit. Under surplus conditions, BES or EL is dispatched to absorb the excess power. The produced hydrogen is then stored in LPHS or HPHS depending on the surplus level. Under deficit conditions, BES or FC is dispatched to compensate for the power shortfall. Hydrogen is correspondingly withdrawn from LPHS or HPHS. Scenario selection follows the maximum membership principle, while satisfying device operating constraints and storage-state constraints.

where $|s_i\rangle$ denotes the quantum basis of each of the four behaviors. α_i denotes the corresponding probability amplitude. φ_i denotes the phase term, which does not affect the selection probability in this paper and is only used to maintain the completeness of the quantum-state representation. α_i satisfies the normalization condition:

$$\sum_{i=1}^{4}\left|\alpha_i\right|^2=1 \tag{29}$$

According to the Born rule, the probability that behavior S_i is invoked in the current iteration is:

$$P_{s_i}=\langle s_i|S\rangle^2=|\alpha_i|^2, i=1,2,3,4. \tag{30}$$

when a behavior S_j is sampled during the iteration and used to generate a new solution, the probability amplitudes are adjusted in the two-dimensional subspace "selected behavior subspace–unselected behavior subspace", which can be expressed as:

$$\begin{cases} |S_j\rangle & =\alpha_j\left|s_j\right\rangle+\widetilde{\alpha}_j\left|\overset{-}{s}_j\right\rangle \\ \widetilde{\alpha}_j & =\sqrt{1-|\alpha_j|^2} \end{cases} \tag{31}$$

where $\left|\overset{-}{s}_j\right\rangle$ denotes the normalized superposition vector of the unselected behavior subspace. $\widetilde{\alpha}_j$ denotes the superposition amplitude of the unselected subspace. $\left|\overset{-}{s}_j\right\rangle$ is calculated as:

$$\left|\overset{-}{s}_j\right\rangle=\frac{\sum_{k\neq j}\alpha_k e^{i\varphi_k}|s_k\rangle}{\sqrt{\sum_{k\neq j}|\alpha_k|^2}} \tag{32}$$

According to the principles of quantum computation, these amplitudes satisfy the normalization condition:

$$|\alpha_j|^2+|\widetilde{\alpha}_j|^2=1 \tag{33}$$

To reinforce behaviors that yield effective improvements and suppress ineffective behaviors, a quantum rotation gate is adopted to update the behavior-selection state in the above two-dimensional subspace:

$$\left|S_j^{new}\right\rangle=R(\Delta\theta)\left|S_j\right\rangle \tag{34}$$

The rotation-gate matrix is:

$$R(\Delta\theta)=\begin{bmatrix}\cos(\Delta\theta) & -\sin(\Delta\theta)\\ \sin(\Delta\theta) & \cos(\Delta\theta)\end{bmatrix} \tag{35}$$

The rotation angle $\Delta\theta$ is jointly determined by the success indicator and the simulated annealing factor, so as to realize the adaptive regulation of "enhancing effective behaviors and weakening ineffective behaviors".

$$\begin{cases} \Delta\theta & =\kappa(t)\cdot(\theta_b-\theta)\cdot rand \\ \theta_b & =\begin{cases}\theta^{max}, & \eta=+1\\ \theta^{min}, & \eta=-1\end{cases} \end{cases} \tag{36}$$

The annealing coefficient is given by:

$$\kappa(t)=\kappa_0\left(1-\frac{t}{T}\right) \tag{37}$$

where t and T denote the current iteration number and the maximum iteration number, respectively. *rand* denotes a random number uniformly distributed in [0,1].

4.2. Adaptive quantum rotation gate update strategy

To provide a unified description of how the iteration process affects the perturbation intensity, a normalized iteration ratio is introduced to construct a decaying annealing term. This enables a smooth transition from global exploration to local exploitation:

$$\tau=\frac{t}{T}\in\left(0,1\right] \tag{38}$$

The foraging behavior mimics the decision-making process of a parrot when searching for food. It jointly considers the current position of the parrot (similar to local optimality) and the food distribution (similar to global exploration information), and then moves toward a position with a better comprehensive evaluation.

$$\begin{cases} \beta_i^{new} & =\sqrt{\varepsilon_1+\varepsilon_2} \\ \varepsilon_1 & =\left|\beta_i^2-\left(\widehat{\beta}_i^s\right)^2\right|\cdot Levy \\ \varepsilon_2 & =rand\cdot e^{-\lambda\cdot\tau}\cdot\left(\widehat{\beta}_i^{all}\right)^2 \end{cases} \tag{39}$$

where ε_1 describes the Levy-flight term relative to the reference state. ε_2 is a random perturbation term decaying with the annealing factor, where $e^{-\lambda\cdot\tau}$ is used to reduce ineffective large-step oscillations in the later stage. The Levy step is generated using the Mantegna sampling scheme, as given in Eq. (40).

$$\begin{cases} Levy & =\dfrac{\mu}{|\nu|^{1/\gamma}} \\ \mu & \sim N\left(0,\sigma_\mu^2\right) \\ \nu & \sim N(0,\sigma_\nu^2) \\ \sigma_\mu & =\left(\dfrac{\Gamma(1+\gamma)\cdot\sin(\pi\gamma/2)}{\Gamma\left(\frac{1+\gamma}{2}\right)\cdot\gamma\cdot2^{(\gamma-1)/2}}\right)^{1/\gamma} \end{cases} \tag{40}$$

The staying behavior is used for local exploitation around the current best region. The update is constructed by a weighted combination of Levy micro-perturbation and random perturbation:

$$\beta_i^{new}=\sqrt{\beta_i^2+\omega_s\left(\widehat{\beta}_i^s\right)^2\cdot Levy+(1-\omega_s)\cdot rand} \tag{41}$$

where $\omega_s\in(0,1)$ controls the balance between local exploitation strength and random perturbation.

The communicating behavior is used to enhance information exchange and diversity diffusion in the population. It switches between two communication modes via the probability threshold p_c:

$$\begin{cases} \beta_i^{new} & =\begin{cases}\sqrt{\varepsilon_3}, & q\le p_c\\ \sqrt{\varepsilon_4}, & q>p_c\end{cases} \\ \varepsilon_3 & =\xi\cdot rand\cdot(1-\tau)\cdot\left|\beta_i^2-\left(\widehat{\beta}_i^{all}\right)^2\right| \\ \varepsilon_4 & =\xi\cdot rand\cdot\exp\left(-\dfrac{s}{rand+\epsilon}\right) \end{cases} \tag{42}$$

where ε_3 is a difference-diffusion term with an annealing component that decays with $(1-\tau)$. ε_4 is an exponential random communication perturbation. ξ denotes the communication diffusion intensity coefficient. ϵ is a small constant introduced to avoid a zero denominator.

The fearing-strangers behavior mimics the action whereby a parrot moves away from a stranger and returns to the group for safety. It is used to realize an escape mechanism from local optima. This is achieved by constructing an antagonism between the "gain term" and the "inhibition term" to enhance robustness:

$$\begin{cases} \beta_i^{new} & = \sqrt{\left|\beta_i^2 + \varepsilon_5 - \varepsilon_6\right|} \\ \varepsilon_5 & = rand \cdot \sin\left(\frac{\pi}{2}(1-\tau)\right) \cdot \left(\left(\hat{\beta}_i^s\right)^2 - \beta_i^2\right) \\ \varepsilon_6 & = \cos\left(2\pi \cdot rand\right) \cdot \left|\beta_i^2 - \left(\hat{\beta}_i^s\right)^2\right| \cdot \tau^2 \end{cases} \tag{43}$$

where ε_5 adopts a sinusoidal modulation term that decays with the iteration ratio to gradually weaken the escape intensity. ε_6 adopts a periodic random inhibition term and introduces τ^2 to promote perturbation convergence. To ensure numerical stability, if overflow or a non-real value appears under the square root, truncation/projection correction is applied to satisfy the variable domain constraints.

4.3. QMOPO workflow

To clearly present the overall solution logic of the proposed QMOPO, Fig. 3 illustrates its complete workflow. Specifically, Eqs. (28)–(30) are used to construct the quantum state for behavioral selection and determine the sampling probabilities of the four behavioral operators. Eqs. (31)–(37) perform the parameterized rotation update in the two-dimensional subspace spanned by the selected and unselected behaviors. Eqs. (38)–(43) govern the position updates corresponding to the foraging, staying, communicating, and fearing-strangers behaviors. In this manner, quantum-inspired behavioral selection, behavior-specific position updating, and evaluation-driven parameter refinement are unified within a single iterative framework.

5. Case study

5.1. Case description and data setup

To verify the effectiveness of the proposed capacity configuration optimization model and solution method for the islanded EH-IES, this paper conducts year-scale simulations based on a typical islanded energy supply system in China (see Table 1). During operation, the system is not connected to the external grid, and the entire load is jointly supplied by WT, PV, and the internal electro–hydrogen hybrid storage units. Hourly time-series data of WT, PV, and actual electricity demand in 2020 are adopted for this region, yielding 8784 samples over the full year (leap year) with a time step of 1 h. The key system parameters are provided in Table 2 [12,15]. Fig. 4 presents the annual power profiles of WT, PV, and the load. As can be observed, renewable generation exhibits pronounced stochastic fluctuations and seasonal variations. It is also temporally mismatched with the load demand, which imposes requirements on the multi-timescale regulation capability of the system from hourly to seasonal horizons.

5.2. Benchmark settings

To comprehensively evaluate the effectiveness of the proposed capacity optimization model, DQT-EMS, and the solution algorithm, this section performs comparative analyses from two perspectives: optimization-algorithm performance and the performance of the resulting capacity configurations.

5.2.1. Optimization-algorithm comparison

Under DQT-EMS and identical system modeling and constraint settings, five multi-objective algorithms are considered for comparison. Accordingly, five cases are defined: Case-1 (MOPSO), Case-2 (MOPO), Case-3 (NSGA-II), Case-4 (MOEA/D), and Case-5 (QMOPO). To ensure a fair comparison, the parameter settings of the five algorithms are kept consistent. The initial population size is set to 30, the maximum number of iterations is 300, and the archive size of non-dominated solutions is 150. All algorithms are executed under the same device parameters (Table 2), constraint conditions, and year-scale simulation environment. The same feasibility-handling mechanism and non-dominated sorting criterion are also adopted.

To enable a comparable evaluation of the Pareto solution sets produced by different algorithms, TOPSIS is employed to select a compromise solution from each solution set for comparison. In the TOPSIS evaluation, the three objectives are unified under the "smaller-is-better" principle for cost, LPSP, and CUR. The weight vector $w = [0.4, 0.3, 0.3]$ is used to perform normalization and compute the distances to the ideal point [35]. The three-objective values and the corresponding capacity configurations of the selected compromise solutions are summarized in Table 3.

As shown in Table 3, the five algorithms exhibit different trade-off patterns across the three objectives. Case-2 (MOPO) achieves the best economic performance, with a total cost of 8.878 million CNY. However, its LPSP reaches 0.24% and its CUR is 1.85%, indicating that the compromise solution is more cost-oriented while the reliability and renewable-energy utilization are relatively weakened. Case-1 (MOPSO) delivers higher reliability, with an LPSP of 0.05%. Its economic performance is the weakest, and the total cost increases to 9.113 million CNY. Meanwhile, the CUR is 1.60%, suggesting that this solution is more conservative in ensuring energy supply at the expense of higher system cost. Case-3 (NSGA-II) and Case-4 (MOEA/D) provide intermediate compromise solutions, but their LPSP and CUR are still higher than those of Case-5. By contrast, Case-5 (QMOPO) provides a more balanced compromise. Its total cost is 8.889 million CNY, which is close to the best cost level of Case-2. The LPSP is reduced to 0.08%, and the CUR is only 0.80%. These results indicate that QMOPO can better enhance renewable-energy utilization at the compromise solution. It also achieves a more reasonable balance between economic performance and supply reliability.

Table 4 and Fig. 5 compare the five algorithms in terms of solution-set quality (HV) and computational cost (runtime). Under the same reference point, the final HV of Case-5 (QMOPO) is 0.019306, which is higher than those of the other four algorithms. These results indicate that the Pareto set produced by QMOPO achieves better overall performance in both convergence and distribution uniformity. Meanwhile, the runtime of QMOPO is 436.28 s, which is lower than those of the other four algorithms. This suggests that QMOPO improves HV without increasing the computational burden, thereby offering higher computational efficiency.

The HV convergence curves in Fig. 5 further reveal the search characteristics of the five algorithms. In Case-1 (MOPSO), HV increases rapidly at the early stage. It then enters a plateau relatively early and exhibits noticeable fluctuations, which implies possible premature convergence and insufficient archive maintenance under complex constraints. In Case-2 (MOPO), the improvement is slower at the beginning. The HV continues to increase in the middle and late stages, and it eventually reaches a relatively high final value, which reflects a certain level of robustness. Case-3 (NSGA-II) shows relatively stable convergence, but its final HV remains lower than that of QMOPO. Case-4 (MOEA/D) increases rapidly at the early stage due to its decomposition-based search mechanism, but its late-stage improvement is limited. By contrast, Case-5 (QMOPO) maintains sustained gains in the middle and late stages and finally attains the highest HV. This indicates that QMOPO can further push the solution set toward a better Pareto front in the later iterations while preserving diversity. As a result, it achieves stronger global search performance and better solution-set quality.

5.2.2. Sensitivity analysis of TOPSIS weight vector

The selection of the TOPSIS compromise solution is affected by the weight vector w. In the benchmark analysis, S2 = [0.40, 0.30, 0.30] is adopted as the TOPSIS weight vector, where the three elements correspond to the weights of TLCC, LPSP, and CUR. Because the proposed capacity configuration model is a long-term planning problem, where system economy is an important concern at the planning stage.

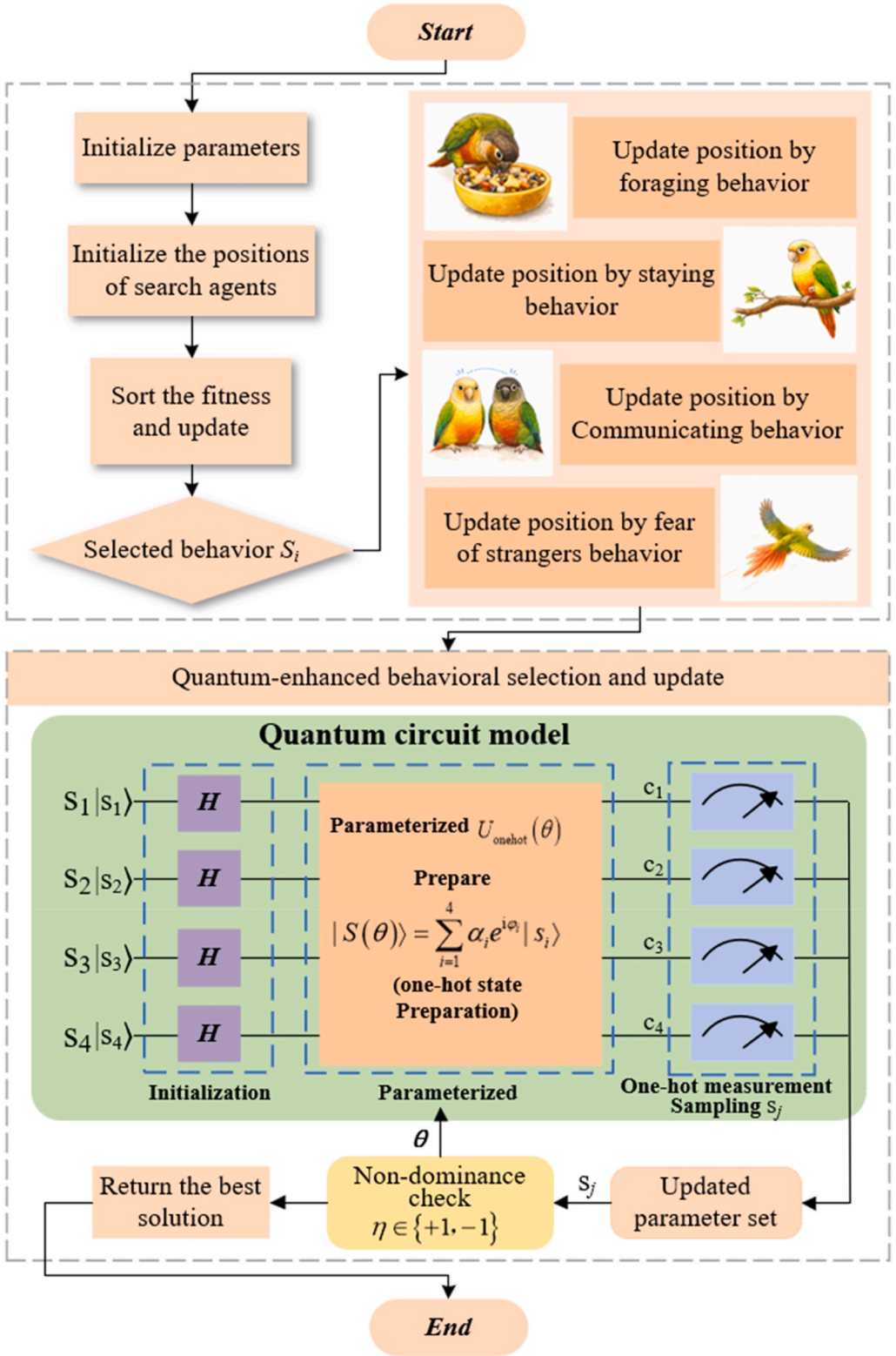


Fig. 3. Flowchart of the proposed QMOPO with quantum-inspired behavioral selection and update. The upper part presents the classical iterative procedure of the parrot optimizer, including parameter initialization, initialization of search-agent positions, fitness ranking, and position updating based on four behavioral operators. The lower part presents the quantum-inspired behavioral selection and parameter updating process, where a behavioral quantum state is constructed through a parameterized quantum circuit, the currently executed behavior is determined via one-hot measurement sampling, and the parameter set is subsequently updated according to the non-dominance evaluation result.

Table 1
Nomenclature.

Abbreviations		$P_{dump}(t)$	Power shortage of the system at time t (kW)
BES	Battery energy storage	$P_{ele}(t)$	EL input power at time t (kW)
CGWO	Continuous grey wolf optimizer	$P_{SC}^{ch}(t)$	BES charging power at time t (kW)
CUR	Renewable energy curtailment rate	$P_{SC}^{dis}(t)$	BES discharging power at time t (kW)
DQT	Dynamic quantum-threshold	$P_{FC,\max}$	Rated power of FC (kW)
DQT-EMS	Dynamic quantum-threshold energy management strategy	$P_{EL,\max}$	Rated power of EL (kW)
EH-IES	Electro-hydrogen integrated energy storage systems	$P_{load}(t)$	Load power at time t (kW)
EL	Electrolyzer	P_i	Rated power of the i-th device (kW)
ELCC	Electricity loapod carrying capacity	$P_{pv}(t)$	PV output power at time t (kW)
FC	Fuel cell	$P_{loss}(t)$	Curtailed renewable power at time t (kW)
HPHS	High-pressure hydrogen storage	$P_{SC}(t)$	Operating power of BES at time t (kW)
HV	Hypervolume	P_r	Rated power of WT (kW)
LCOE	Levelized cost of electricity	P_{STC}	Rated PV power under STC (kW)
LPHS	Low-pressure hydrogen storage	$P_{SC,\max}$	Rated power of BES (kW)
LPSP	Loss of power supply probability	r	Discount rate
MOPO	Multi-objective parrot optimization.	$P_{wt}(t)$	WT output power at time t (kW)
MOPSO	Multi-objective particle swarm optimization	$SOC_{H_2}(t)$	Hydrogen storage state at time t
PSO-WD	Particle swarm optimization-wavelet decomposition	$T_a(t)$	Actual temperature at time t (°C)
QBWO	Quantum beluga whale optimization	$SOC_{SC}(t)$	State of charge of BES at time t
QMOPO	Quantum multi-objective parrot optimization	T_{STC}	Temperature under STC (°C)
SOC	State of charge	$T_{amb}(t)$	Ambient temperature at time t (°C)
STC	Standard test conditions	v_{in}	Cut-in wind speed (m/s)
Parameters		$v(t)$	Wind speed at hub height at time t (m/s)
$\alpha(t)$	Relative contribution coefficient of BES in constructing the dynamic threshold	v_r	Rated wind speed (m/s)
$\beta(t)$	Relative contribution coefficient of EL in constructing the dynamic threshold	v_{out}	Cut-out wind speed (m/s)
$\gamma(t)$	Relative contribution coefficient of FC in constructing the dynamic threshold	$\eta_{ch,high}$	Hydrogen charging efficiency of HPHS
γ_{high}	Leakage loss rate of HPHS	$\eta_{ch,SC}$	Charging energy loss rate of BES
γ_{low}	Leakage loss rate of LPHS	$\eta_{dis,SC}$	Discharging energy loss rate of BES
$c_{e,i}$	Unit capacity cost of the i-th device	η_{ch,H_2}	Hydrogen charging efficiency
$c_{p,i}$	Unit power cost of the i-th device	η_{dis,H_2}	Hydrogen discharging (release) efficiency
C_{cap}	capital cost (CNY)	η_{fc}	Conversion efficiency of FC
C_{om}	Operation and maintenance cost (CNY)	η_{ele}	Electrolysis efficiency
C_{rep}	Equipment replacement cost (CNY)	ω	Weighting coefficient of an individual objective
E_{SC}^{cap}	Rated energy capacity of BES (kWh)	ε_6	Periodic random modulation term
E_i	Capacity of the i-th device (kWh)		

Table 2
Technical and economic parameters of each unit in the islanded EH-IES.

Unit	Initial investment	Operating cost ratio	Service life
PV	4500(CNY/kW)	2%	25years
WT	5200(CNY/kW)	2%	20years
EL	6000(CNY/kW)	3%	15years
FC	12000(CNY/kW)	3%	15years
BES	2000(CNY/kWh)	1%	10years
LPHS	3000(CNY/KG)	2%	15years
HPHS	5000(CNY/KG)	2%	15years

Meanwhile, the supply reliability and renewable energy utilization of the islanded system also significantly affect system operation [35]. Therefore, LPSP and CUR are also assigned relatively high weights. On this basis, seven typical preference weight combinations are further selected to analyze the sensitivity of compromise-solution selection under different decision preferences.

As shown in Fig. 6, different weight combinations lead TOPSIS to select different compromise solutions from the Pareto solution set. When the weight of TLCC is increased, the selected solution tends to move toward the low-cost region. When the weight of LPSP is increased, the selected solution tends to move toward the high-reliability region. When the weight of CUR is increased, the selected solution tends to move toward the low-curtailment region. This indicates that the weight vector can reflect different decision preferences for economy, supply reliability, and renewable energy utilization. It also affects the capacity configuration results of key storage devices, such as BES, LPHS, and HPHS.

Overall, the compromise solutions obtained under the balanced weight and slightly biased weights are relatively close to each other. This indicates that the TOPSIS selection result has a certain stability under small weight variations. When the weight of one objective is further increased, the position of the selected compromise solution changes more clearly. This means that a stronger decision preference has a more significant impact on the final capacity configuration. Therefore, the proposed framework can flexibly select compromise solutions according to different engineering requirements. It provides decision support for balancing economy, reliability, and renewable energy accommodation.

5.2.3. Comparative analysis of decision schemes

To further evaluate the impact of the proposed DQT-EMS on capacity configuration and operational performance, this paper compares two operating strategies under the same optimization framework and the same solution algorithm (QMOPO). The two strategies are Case-5 (DQT-EMS) and Case-6 (priority-based EMS). For both strategies, capacity configuration optimization is performed for the islanded EH-IES under the same device parameters and constraint settings, and the corresponding Pareto solution sets are obtained. A unified TOPSIS method is then applied to each solution set to select a compromise solution for comparison. The selected compromise solutions under the two strategies are reported in Table 5.

As shown in Table 5, the two strategies exhibit clear multi-objective trade-offs. Compared with Case-6 (priority-based EMS), Case-5 (DQT-EMS) performs better in terms of economic and environmental objectives. The total cost decreases from 8.909 to 8.889 million CNY, and the curtailment rate is substantially reduced from 2.49% to 0.80%. These results indicate that the dynamic-threshold strategy can more effectively guide storage and energy-conversion devices to participate in regulation, which enhances renewable-energy utilization and reduces the overall system cost. Meanwhile, the LPSP of Case-5 is 0.08%, which is higher than the 0.01% of Case-6. This suggests that, under the selected compromise solutions, the dynamic-threshold strategy tends to achieve a more balanced capacity and operational outcome between "stringent reliability assurance" and "cost–utilization improvement." Overall, by providing a more consistent triggering scale for decision making, DQT-EMS helps strengthen the coordinated dispatch among BES, dual-

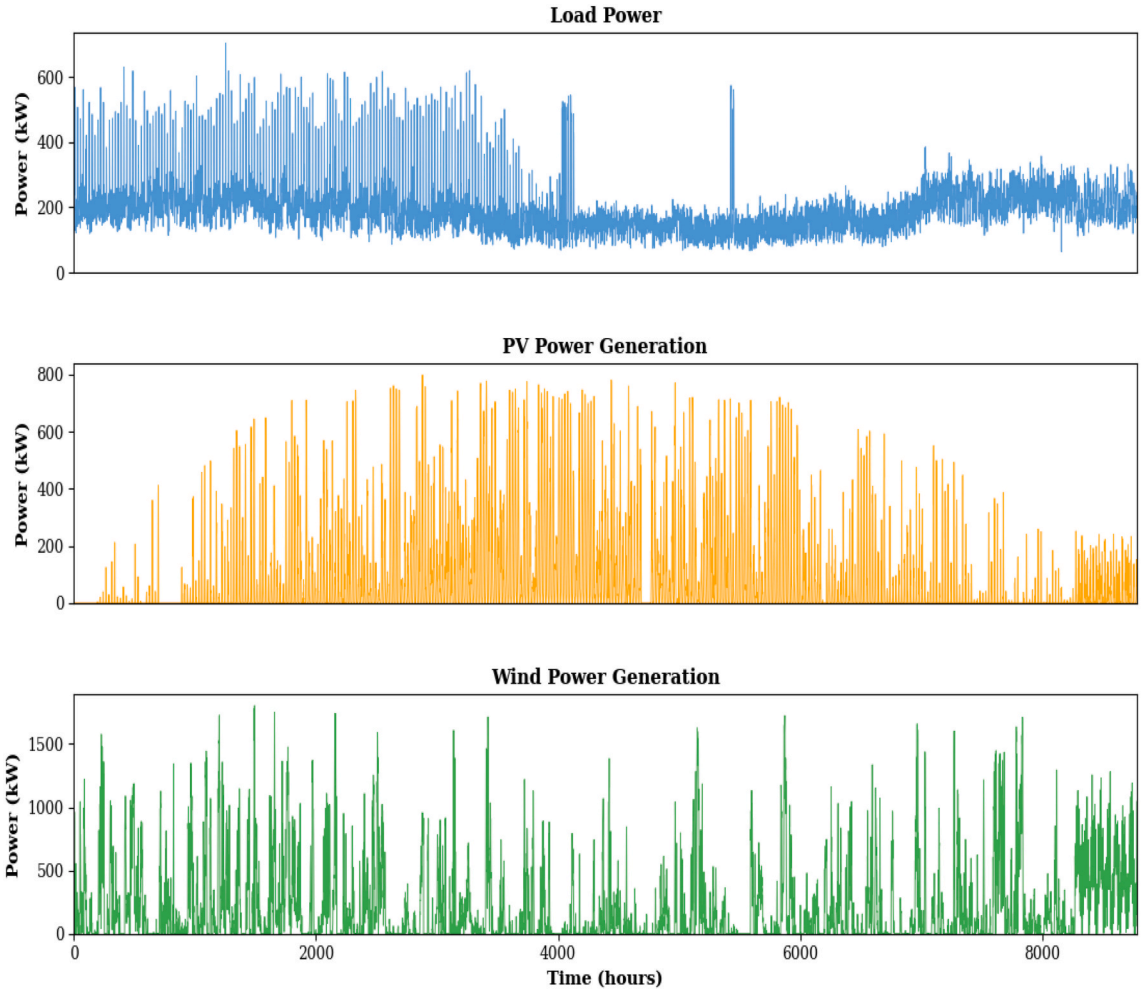


Fig. 4. Annual power profiles of WT, PV, and load.

Table 3
Comparison of capacity configurations obtained by different optimization algorithms.

Case	TLCC (million CNY)	LPSP	CUR	BES (kWh)	LPHS (KG)	HPHS (KG)
Case-1	9.113	0.05%	1.60%	959	3796	3324
Case-2	8.878	0.24%	1.85%	963	2939	3732
Case-3	8.956	0.11%	1.12%	1085	3610	3155
Case-4	8.914	0.17%	1.28%	1018	3345	3450
Case-5	8.889	0.08%	0.80%	1192	3989	2890

Table 4
Comparison of algorithm performance (Runtime and HV).

Case	Runtime(s)	HV
Case-1	495.26	0.018093
Case-2	453.60	0.019013
Case-3	528.64	0.018746
Case-4	444.91	0.018902
Case-5	436.28	0.019306

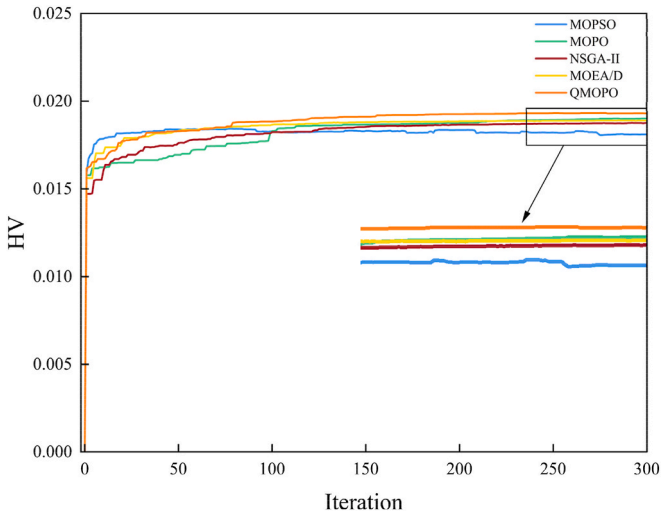


Fig. 5. Convergence curve of HV versus iteration number.

pressure hydrogen storage, and EL/FC. As a result, it improves the overall system performance under multiple objectives.

Figs. 7 and 8 present the annual state trajectories of BES, LPHS, and HPHS in the islanded EH-IES under the DQT-EMS (Case-5) and the priority-based EMS (Case-6), respectively. In both cases, the three

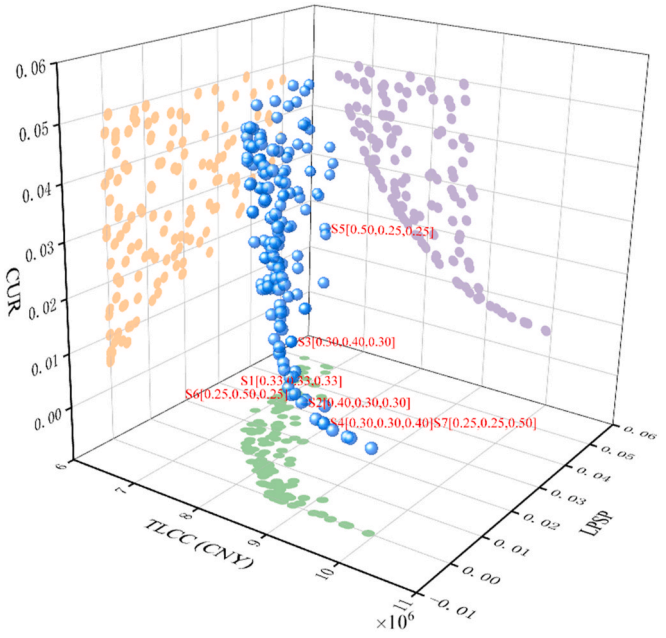


Fig. 6. Pareto front obtained by QMOPO.

Table 5
Comparison of capacity Configuration for DQT-EMS and priority-based EMS.

Case	TLCC (million CNY)	LPSP	CUR	BES (kWh)	LPHS (KG)	HPHS (KG)
Case-5	8.889	0.08%	0.80%	1192	3989	2890
Case-6	8.909	0.01%	2.49%	871	3825	3099

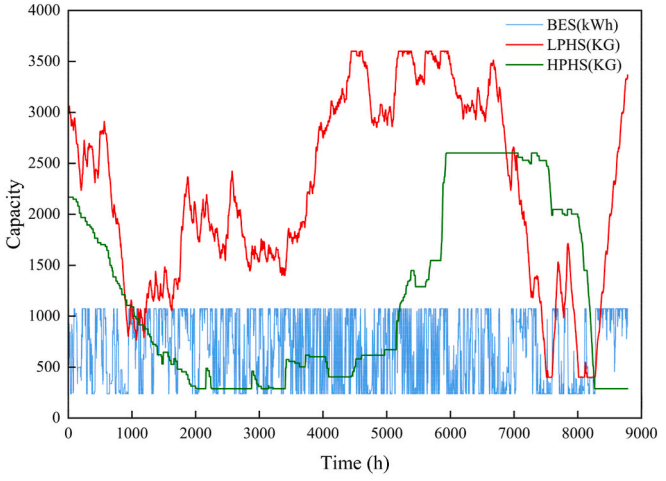


Fig. 7. Annual capacity-variation profiles for Case-5.

storage units exhibit a clear multi-timescale division of labor. BES shows high-frequency fluctuations and mainly provides short-timescale power balancing. LPHS undergoes more frequent staged charging and discharging, indicating its major role in weekly to monthly energy regulation. By contrast, HPHS varies more slowly over the year and mainly serves as seasonal storage for long-term energy shifting. This pressure-level difference enables LPHS and HPHS to play complementary roles in the optimization objectives. LPHS has a lower unit capacity cost and reduces short-term renewable energy curtailment through frequent

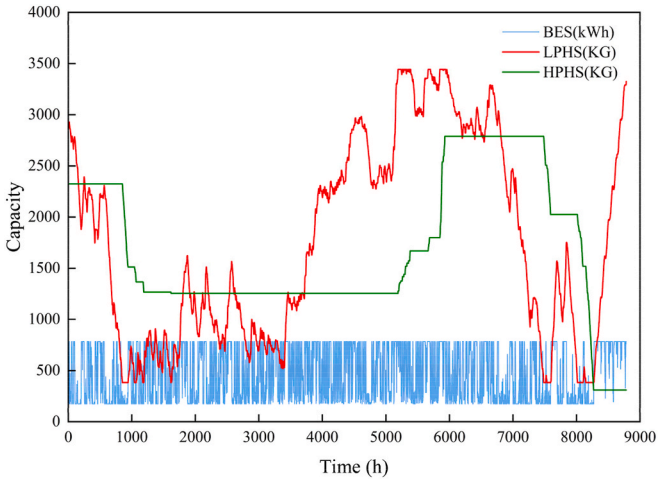


Fig. 8. Annual capacity-variation profiles for Case-6.

short- and medium-term buffering, while HPHS serves as a key storage unit for seasonal energy shifting despite its higher unit capacity cost. Therefore, HPHS improves energy accommodation during renewable generation peaks and enhances long-duration supply reliability. These trajectories indicate that BES, LPHS, and HPHS can operate in a coordinated and hierarchical manner to address energy mismatches over different timescales.

A comparison between Case-5 and Case-6 further reveals the influence of the energy management strategy on storage coordination. In Case-5, BES mainly performs high-frequency and small-amplitude adjustments, which suggests a stronger short-timescale balancing role. In Case-6, BES is more deeply involved in short-term compensation during some deficit periods under the rigid priority rule. LPHS plays a similar mid-term regulation role in both cases, whereas the HPHS trajectory differs more clearly between the two strategies. In Case-6, HPHS exhibits more pronounced stage-wise changes, indicating a more passive activation pattern when LPHS becomes constrained or system deficits increase. In contrast, the HPHS trajectory in Case-5 is smoother and more orderly, which reflects better coordination between the two hydrogen-storage levels and a clearer seasonal energy-shifting characteristic.

Table 6 reports the operating statistics of EL and FC under the two energy management strategies, including the number of start-stop events, total operating hours, and the average operating duration per cycle. These indicators are used to evaluate the dispatching effect of DQT-EMS and the operational continuity of key hydrogen-conversion devices. The results indicate that Case-5 provides better operational continuity than Case-6.

For EL, the number of start-stop events in Case-5 decreases from 421 to 396, which corresponds to a reduction of about 5.9%. The total operating hours increase from 2474 h to 2838 h, which yields an additional 364 h. The average operating duration per cycle rises from 5.88 h to 7.17 h, representing an improvement of about 21.9%. These results suggest that, with dynamic-threshold triggering, EL tends to operate with fewer start-stop events while maintaining longer individual operating intervals. This helps mitigate operational fluctuations caused by frequent switching. It also improves operational stability and dispatch controllability.

For FC, the number of start-stop events in Case-5 decreases from 574 to 424, which corresponds to a reduction of about 26.1%. The average operating duration per cycle increases from 5.82 h to 7.36 h, representing an improvement of about 26.5%. Although the total operating hours of FC in Case-5 are slightly lower than those in Case-6, Case-5 achieves longer continuous operating segments with fewer start-stop events. This indicates that the strategy can reduce fragmented power output and smooth FC operation.

Table 6
Operational statistics of EL and FC.

Case	Number of EL start-stop events	Total EL operating hours	Average EL operating duration per cycle	Number of FC start-stop events	Total FC operating hours	Average FC operating duration per cycle
Case-5	396	2838	7.17	424	3122	7.36
Case-6	421	2474	5.88	574	3338	5.82

Overall, DQT-EMS reduces the switching frequency of key devices by providing a more reasonable power triggering and allocation mechanism. It also significantly extends the continuous operating duration of each cycle. These changes lead to a more stable operational process. They further provide behavioral evidence for explaining the hierarchical coordination mechanism of "BES–LPHS–HPHS" in the subsequent analysis of representative 72-h seasonal periods.

5.2.4. Analysis of typical periods in four seasons

To reveal the operating mechanism of DQT-EMS in inter-seasonal regulation, this paper performs a refined analysis based on the compromise capacity configuration of Case-5. Specifically, four representative 72-h periods are selected for spring, summer, autumn, and winter, respectively. These typical periods are chosen according to the principle of representing net-power fluctuation characteristics. Figs. 9–11 present the WT/PV output, load demand, EL/FC power, and the SOC trajectories of BES, LPHS, and HPHS during the typical periods in the four seasons.

The results of the four representative 72-h periods in spring, summer, autumn, and winter show that the system forms a stable hierarchical regulation pattern across seasons. BES is responsible for fast hourly power balancing. LPHS provides energy buffering from intra-day to intra-week timescales. HPHS ensures long-duration energy adequacy for inter-seasonal regulation.

In spring and other transition seasons, renewable generation and load demand exhibit stage-wise mismatches. The system mainly relies on high-frequency charging/discharging of BES to smooth short-term fluctuations. Surplus power drives EL to produce hydrogen, which is preferentially stored in LPHS. HPHS remains largely stable during this period.

In summer, PV peaks are more concentrated and the surplus power becomes more pronounced. EL is therefore activated more frequently for hydrogen production. The system shows a typical intra-day cycle, where surplus power in daytime is absorbed through hydrogen production and battery charging, while deficits at night are compensated by battery discharging and FC generation. On the hydrogen side, the SOC variations are dominated by mild oscillations of LPHS, and HPHS participates less.

In autumn, WT and PV are complementary, but the fluctuations become more fragmented. BES continues to provide fast regulation, and

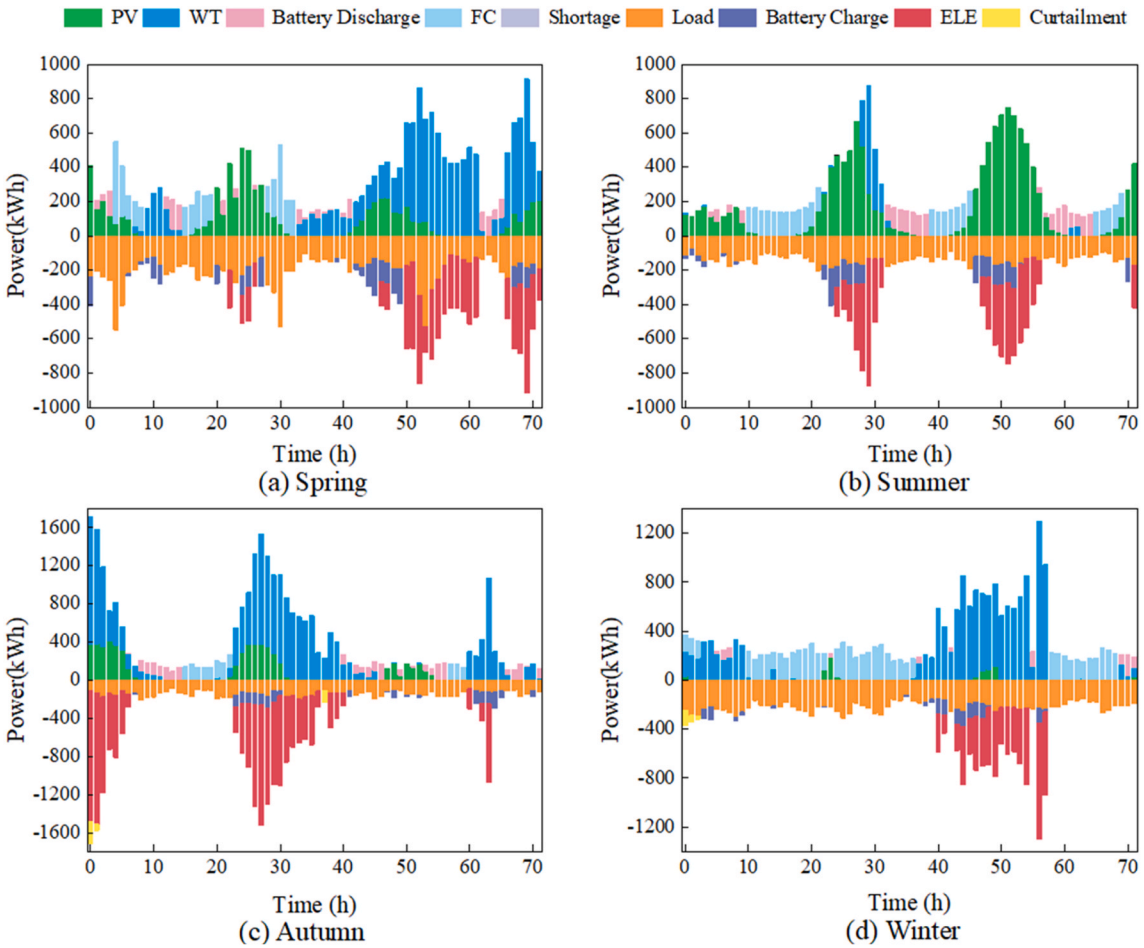


Fig. 9. Energy supply-demand profiles during typical periods in four seasons.

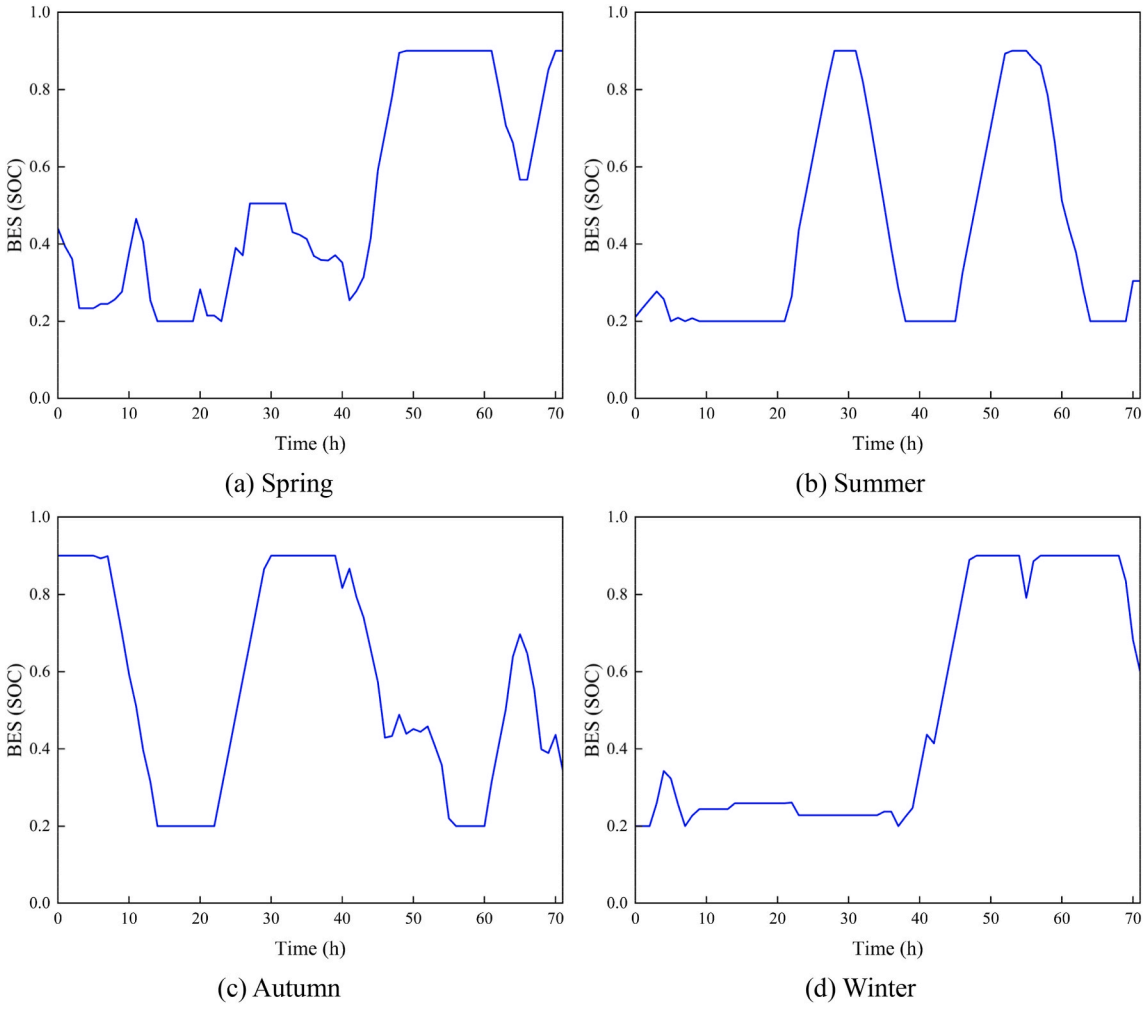


Fig. 10. BES SOC profiles during typical periods in four seasons.

LPHS exhibits a net-charging or staircase-like increasing trend, which indicates an accumulation-oriented stage. HPHS remains relatively stable.

In winter, energy supply becomes tighter and prolonged deficits are more prominent. The continuous output of FC, together with the fast compensation of BES, ensures supply continuity. During this period, HPHS shows a clear discharge process, which highlights its core role in inter-seasonal support. Meanwhile, LPHS charges and discharges at the intra-week scale to buffer short-term fluctuations, which reduces the need to frequently call on HPHS.

Overall, through the hierarchical coordination of "BES–LPHS–HPHS," the system achieves a closed-loop regulation process. This process spans from short-term fluctuation suppression to long-duration energy shifting.

6. Conclusion

This paper investigates an islanded EH-IES and develops a coupled capacity-operation optimization framework. Within this framework, DQT-EMS and QMOPO are proposed. Specifically, DQT-EMS is designed to enhance the coordinated operation of key devices over multiple timescales, whereas QMOPO is employed to solve the high-dimensional multi-objective capacity configuration problem. Year-scale simulations are further conducted to evaluate the proposed method from the perspectives of operational performance and algorithmic performance.

From the operational perspective, DQT-EMS achieves a better trade-off between economic performance and renewable energy utilization, while improving the operating continuity of key devices. Under the same solution algorithm, the compromise solution obtained with DQT-EMS increases the renewable energy utilization rate to 99.20%, while slightly reducing the total cost. In addition, the start-stop count of the electrolyzer decreases by about 5.94%, and that of the fuel cell decreases by about 26.13%, while the average operating duration per cycle of both devices increases to approximately 7 h. These results indicate that DQT-EMS can alleviate fragmented dispatch and enable smoother and more stable system operation.

At the capacity configuration level, QMOPO demonstrates superior overall performance. Under identical parameter settings, the hypervolume (HV) obtained by QMOPO is 6.70% higher than that of MOPSO. Compared with MOPO, the runtime decreases from 453.60 s to 436.28 s, corresponding to a reduction of 3.82%. Moreover, the HV convergence curves indicate that QMOPO can continuously improve the quality of the solution set during the middle and late stages of iteration, thereby obtaining a more stable and more uniformly distributed Pareto front while maintaining computational efficiency.

This study still has limitations, as it mainly considers a small-scale islanded EH-IES with partly idealized scenario boundaries and device parameters. Although the operation and maintenance cost has been included in the total life-cycle cost model, the start-stop costs and lifetime degradation mechanisms of EL and FC are not separately modeled in this study. Future work will extend the proposed framework to larger community microgrids and more complex multi-energy systems, while further refining LPHS/HPHS pressure matching, incorporating degradation-aware modeling of hydrogen conversion devices,

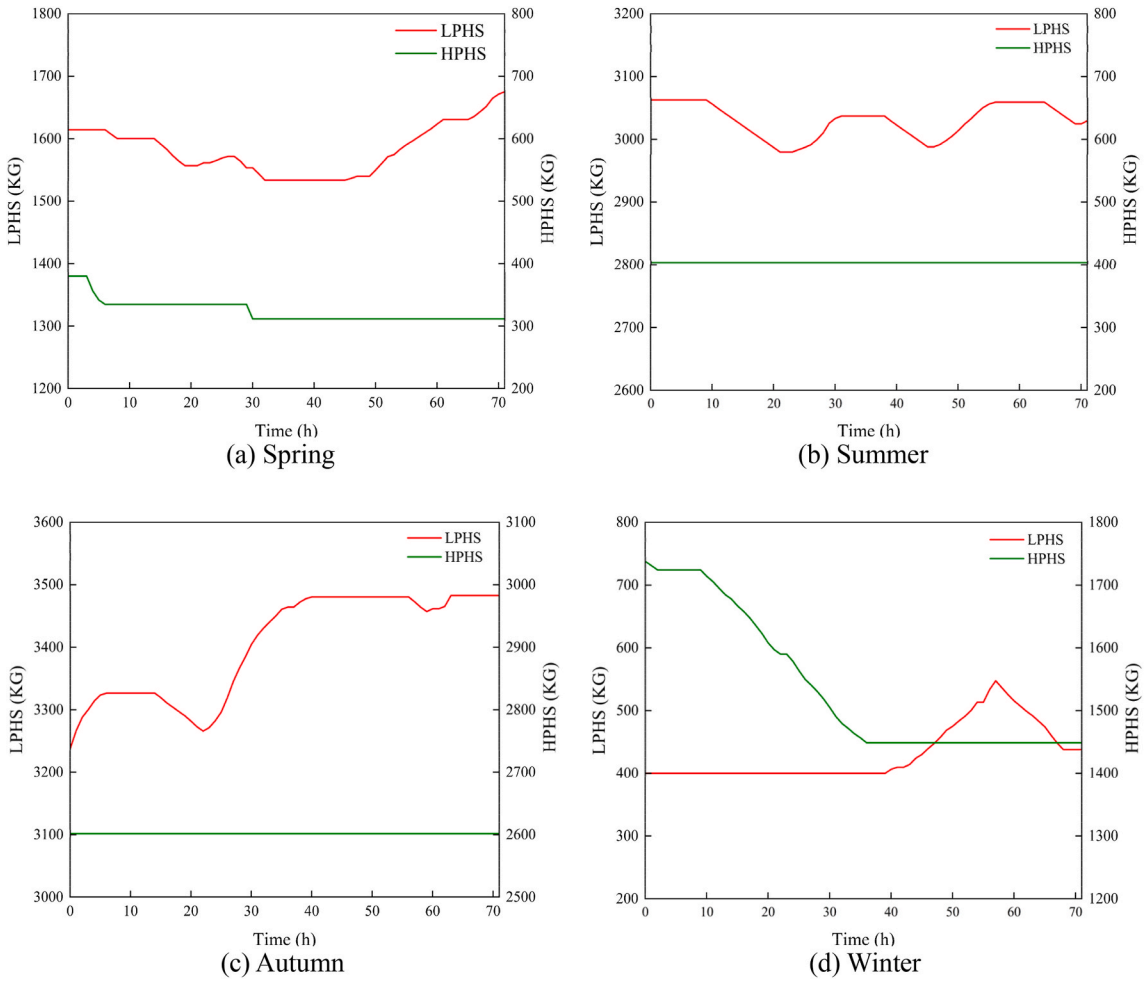


Fig. 11. LPHS and HPHS SOC profiles during typical periods in four seasons.

conducting sensitivity analysis and co-optimization of DQT-EMS parameters, and improving the robustness of the quantum optimization algorithm under complex constraints.

CRediT authorship contribution statement

Shizhao Wang: Writing – review & editing, Writing – original draft, Software, Methodology, Investigation, Data curation, Conceptualization. **Zhenhao Weng:** Writing – review & editing, Investigation. **Ruichong Li:** Writing – review & editing, Investigation. **Longze Wang:** Writing – review & editing, Methodology, Investigation, Funding acquisition, Formal analysis, Conceptualization. **Jingren Zhou:** Writing – review & editing. **Zhehan Li:** Writing – review & editing. **Meicheng Li:** Validation, Supervision, Resources, Project administration, Methodology, Investigation, Funding acquisition.

Declaration of competing interest

The authors declare that they have no known competing financial interests or personal relationships that could have appeared to influence the work reported in this paper.

Acknowledgments

This work is supported partially by Beijing Natural Science Foundation (L2609008), 2022 Strategic Research Key Project of Science and Technology Commission of the Ministry of Education, Beijing Science and Technology Project (Z211100004621010), the project of China Three Gorges Corporation named key technologies of intelligent joint regulation and operation with grid connected friendly in power station group of wind, solar photovoltaic and energy storage (WWKY-2021-0173), Huaneng Group Headquarters Science and Technology Project (HNKJ20-H88), State Key Laboratory of Alternate Electrical Power System with Renewable Energy Sources (LAPS25002), the Fundamental Research Funds for the Central Universities (2025MS048) and the NCEPU Double First-Class Program.

References

[1] Zhou Y, Min C, Wang K, et al. Optimization of integrated energy systems considering seasonal thermal energy storage. J Energy Storage 2023;71:108094. https://doi.org/10.1016/j.est.2023.108094.
[2] Yan R, Wang J, Huo S, et al. Flexibility improvement and stochastic multi-scenario hybrid optimization for an integrated energy system with high-proportion renewable energy. Energy 2023;263:125779. https://doi.org/10.1016/j.energy.2022.125779.
[3] Liu N, Zhang K, Zhang K. Coordinated configuration of hybrid energy storage for electricity-hydrogen integrated energy system. J Energy Storage 2024;95:112590. https://doi.org/10.1016/j.est.2024.112590.
[4] Qiu Y, Li Q, Li S, et al. Lifecycle collaborative planning for traction power supply systems with integrated energy access. IEEE Trans Transp Electrif 2025;11:5055–68. https://doi.org/10.1109/TTE.2024.3476169.
[5] Hu Y, Yang B, Wu P, et al. Optimal planning of electric-heating integrated energy system in low-carbon park with energy storage system. J Energy Storage 2024;99:113327. https://doi.org/10.1016/j.est.2024.113327.
[6] Gu Y, Wei Z, Zhou Y, et al. Robust resiliency-oriented planning of electricity-hydrogen island energy systems under contingency uncertainty. J Clean Prod 2024;476:143678. https://doi.org/10.1016/j.jclepro.2024.143678.
[7] Liu X, Zu L, Wei Z, et al. Two-layer optimal scheduling of integrated electric-hydrogen energy system with seasonal energy storage. Int J Hydrogen Energy 2024;82:1131–45. https://doi.org/10.1016/j.ijhydene.2024.07.415.

[8] Kong H, Sun Y, Li Z, et al. The development path of direct coal liquefaction system under carbon neutrality target: coupling green hydrogen or CCUS technology. Appl Energy 2023;347:121451. https://doi.org/10.1016/j.apenergy.2023.121451.
[9] Wang H, Xie Z, Pu L, et al. Energy management strategy of hybrid energy storage based on Pareto optimality. Appl Energy 2022;327:120095. https://doi.org/10.1016/j.apenergy.2022.120095.
[10] Li Q, Wang Z, Lai H, et al. Optimal scheduling method for integrated energy system considering hydrogen trading and transportation. eTransportation 2026;27:100526. https://doi.org/10.1016/j.etran.2025.100526.
[11] Wang G, Blondeau J. Optimal combination of daily and seasonal energy storage using battery and hydrogen production to increase the self-sufficiency of local energy communities. J Energy Storage 2024;92:112206. https://doi.org/10.1016/j.est.2024.112206.
[12] Li Z, Xia Y, Bo Y, et al. Optimal planning for electricity-hydrogen integrated energy system considering multiple timescale operations and representative time-period selection. Appl Energy 2024;362:122965. https://doi.org/10.1016/j.apenergy.2024.122965.
[13] Kannaiyan K, Lekshmi GS, Ramakrishna S, et al. Perspectives for the green hydrogen energy-based economy. Energy 2023;284:129358. https://doi.org/10.1016/j.energy.2023.129358.
[14] Abe JO, Popoola API, Ajenifuja E, et al. Hydrogen energy, economy and storage: review and recommendation. Int J Hydrogen Energy 2019;44:15072–86. https://doi.org/10.1016/j.ijhydene.2019.04.068.
[15] Bouaouda A, Sayouti Y. An optimal sizing framework of a microgrid system with hydrogen storage considering component availability and system scalability by a novel approach based on quantum theory. J Energy Storage 2024;92:111894. https://doi.org/10.1016/j.est.2024.111894.
[16] Song Q, Wang B, Wang Z, et al. Multi-objective capacity configuration optimization of the combined wind-storage system considering ELCC and LCOE. Energy 2024;301:131558. https://doi.org/10.1016/j.energy.2024.131558.
[17] Wei D, He M, Zhang J, et al. Enhancing the economic efficiency of wind-photovoltaic-hydrogen complementary power systems via optimizing capacity allocation. J Energy Storage 2024;104:114531. https://doi.org/10.1016/j.est.2024.114531.
[18] Zhang W, Zhang M, Liu J. Optimal multi-energy storage capacity allocation for electricity-heat-hydrogen-ammonia integrated energy systems with ammonia cycling. Renew Energy 2026;257:124788. https://doi.org/10.1016/j.renene.2025.124788.
[19] Wei M, Chen J, Zhang W, et al. Two-layer multi-timescale rolling optimization of electric-hydrogen hybrid energy storage systems considering renewable energy uncertainties. Int J Hydrogen Energy 2025;106:305–17. https://doi.org/10.1016/j.ijhydene.2025.01.435.
[20] Tang D, Yuan Y, Ge P, et al. A framework for multi-objective optimization of hybrid energy storage in integrated multi-energy systems at mega seaports. J Energy Storage 2025;120:116452. https://doi.org/10.1016/j.est.2025.116452.
[21] Ibáñez-Rioja A, Järvinen L, Puranen P, et al. Off-grid solar PV–wind power–battery–water electrolyzer plant: simultaneous optimization of component capacities and system control. Appl Energy 2023;345:121277. https://doi.org/10.1016/j.apenergy.2023.121277.
[22] Zhao Y, Zhao Y, Cao S, et al. Capacity configuration and control optimization of off-grid wind solar hydrogen storage system. Energy 2025;324:136002. https://doi.org/10.1016/j.energy.2025.136002.
[23] Wang Z, Xu C, Yu B, et al. Multi-objective optimization of capacity configuration in a wind–PV–compressed air energy storage hybrid system. Energy 2025;332:137097. https://doi.org/10.1016/j.energy.2025.137097.
[24] Han X, Li J, Zhang Z. Dynamic game optimization control for shared energy storage in multiple application scenarios considering energy storage economy. Appl Energy 2023;350:121801. https://doi.org/10.1016/j.apenergy.2023.121801.
[25] Ren Z, Yu Q, Lin D, et al. Optimal capacity configuration of a wind-solar-battery-diesel microgrid system using continuous grey wolf optimization. J Energy Storage 2025;113:115630. https://doi.org/10.1016/j.est.2025.115630.
[26] Ma X, Deveci M, Yan J, et al. Optimal capacity configuration of wind-photovoltaic-storage hybrid system: a study based on multi-objective optimization and sparrow search algorithm. J Energy Storage 2024;85:110983. https://doi.org/10.1016/j.est.2024.110983.
[27] Zhang X, Zhang H, Zhang L, et al. Optimization of a wind-PV-hydrogen production coupling system considering economy, environment, and reliability. Int J Hydrogen Energy 2025;105:441–57. https://doi.org/10.1016/j.ijhydene.2025.01.295.
[28] Liu L, Zhai R, Hu Y. Multi-objective optimization with advanced exergy analysis of a wind-solar-hydrogen multi-energy supply system. Appl Energy 2023;348:121512. https://doi.org/10.1016/j.apenergy.2023.121512.
[29] Qiao J, Mi Y, Shen J, et al. Optimization schedule strategy of active distribution network based on microgrid group and shared energy storage. Appl Energy 2025;377:124681. https://doi.org/10.1016/j.apenergy.2024.124681.
[30] Wang X, Geng Z, Chen L, et al. Improved dragonfly optimization algorithm based on quantum behavior for multi-objective optimization of ethylene cracking furnace. Swarm Evol Comput 2024;88:101607. https://doi.org/10.1016/j.swevo.2024.101607.
[31] Zhu S, Du B, Lu X, et al. Design and optimization of a cascade hydrogen storage system for integrated energy utilization. J Energy Storage 2024;96:112732. https://doi.org/10.1016/j.est.2024.112732.
[32] Xiao L, Chen J, Wu Y, et al. Effects of pressure levels in three-cascade storage system on the overall energy consumption in the hydrogen refueling station. Int J Hydrogen Energy 2021;46:31334–45. https://doi.org/10.1016/j.ijhydene.2021.07.007.
[33] Teo TT, Logenthiran T, Woo WL, et al. Optimization of fuzzy energy-management system for grid-connected microgrid using NSGA-II. IEEE Trans Cybern 2021;51:5375–86. https://doi.org/10.1109/TCYB.2020.3031109.
[34] Lian J, Hui G, Ma L, et al. Parrot optimizer: algorithm and applications to medical problems. Comput Biol Med 2024;172:108064. https://doi.org/10.1016/j.compbiomed.2024.108064.
[35] Punyam Rajendran SS, Gebremedhin A. Holistic planning framework for multi-energy microgrids: a multi-objective perspective on system optimization. Appl Energy 2025;392:125953. https://doi.org/10.1016/j.apenergy.2025.125953.